Creation of a novel trigeminal tractography atlas for automated trigeminal nerve identification

Fan Zhang[1], Guoqiang Xie[1,2], Laura Leung[1,3,4], Michael A. Mooney[3], Lorenz Epprecht[5], Isaiah Norton[1], Yogesh Rathi[1,6], Ron Kikinis[1], Ossama Al-Mefty[3], Nikos Makris[6,7], Alexandra J. Golby[1,3], Lauren J. O'Donnell[1]

1 Department of Radiology, Brigham and Women's Hospital, Harvard Medical School, Boston, USA
2 Department of Neurosurgery, Nuclear Industry 215 Hospital of Shaanxi Province, Xianyang, China
3 Department of Neurosurgery, Brigham and Women's Hospital, Harvard Medical School, Boston, USA
4 Faculty of Medicine, The Chinese University of Hong Kong, Hong Kong, China
5 Department of Otolaryngology, Head and Neck Surgery, University Hospital Zurich, Zurich, Switzerland
6 Department of Psychiatry, Brigham and Women's Hospital, Harvard Medical School, Boston, USA
7 Departments of Psychiatry, Neurology and Radiology, Massachusetts General Hospital, Harvard Medical School, Boston, USA

Abstract

Diffusion MRI (dMRI) tractography has been successfully used to study the trigeminal nerves (TGNs) in many clinical and research applications. Currently, identification of the TGN in tractography data requires expert nerve selection using manually drawn regions of interest (ROIs), which is prone to inter-observer variability, time-consuming and carries high clinical and labor costs. To overcome these issues, we propose what we believe is the first study for automated identification of the TGN from dMRI tractography. In this paper, we first illustrate the creation of a trigeminal tractography atlas. Leveraging a well-established computational pipeline, we generate a data-driven TGN fiber clustering atlas using tractography data from 50 subjects from the Human Connectome Project. Expert neuroanatomical knowledge is used for anatomical curation of the TGN in the atlas. Then, we demonstrate the application of the proposed atlas for automated TGN identification in new subjects from two different acquisition sites. Quantitative and visual experiments are performed with comparison to expert TGN identification. We show highly comparable results between the automatically and manually identified TGNs in terms of spatial overlap and visualization, while our proposed method has several advantages. First, our method performs automated TGN identification, and thus it provides an efficient tool to reduce expert labor costs and inter-operator bias relative to expert manual selection. Second, our method is robust to potential imaging artifacts and/or noise that prevented successful manual ROI placement for TGN selection and hence yields higher successful TGN identification rate.

1. Introduction

The trigeminal nerve (TGN) is the largest and most complex of the 12 pairs of cranial nerves in the brain. It supplies sensation to the skin in the face, the ear, the mucous membranes orally and endonasally as well as motor innervation to the muscles of mastication. The TGN has been shown to be affected in many diseases such as trigeminal neuralgia (Jannetta 1967), multiple sclerosis (Love and Coakham 2001; Yadav et al. 2017), local ischemia (Delitala, Brunori, and Chiappetta 1999; Balestrino and Leandri 1997; Golby, Norbash, and Silverberg 1998) and brain cancer (Timothee Jacquesson et al. 2019). Many research studies have also suggested that the identification of TGN is important for understanding and/or potential treatment of various neurological disorders such as major depressive disorder (Schrader et al. 2011), attention-deficit/hyperactivity disorder (McGough et al. 2015), and Parkinson's disease (Barz et al. 1997).

Magnetic resonance imaging (MRI) techniques have been used to identify the TGN for clinical and research purposes (Tsutsumi et al. 2018; N. Yoshino et al. 2003; Ruiz-Juretschke et al. 2018; Ciftci et al. 2004; Casselman et al. 2008; Timothee Jacquesson et al. 2019). In particular, diffusion MRI (dMRI), via a process called tractography, can track brain white matter and nerve fibers in vivo non-invasively based on the principle of detecting the random motion of water molecules in neural tissue (Basser et al. 2000; Basser, Mattiello, and LeBihan 1994). dMRI tractography has been applied successfully for tracking of the TGN (M. Yoshino et al. 2016; Fujiwara et al. 2011; Ishida et al. 2011; Wei et al. 2016; Timothée Jacquesson et al. 2018; Hung et al. 2017). One advantage of dMRI tractography is that it enables tracking of the 3D trajectory of the TGN for visualization of TGN structures not visualized by conventional MRI sequences (e.g., T2-weighted image, T2w), e.g. the course of the TGN within the brainstem as well as anterior to the cisternal portion (Timothée Jacquesson et al. 2018; Xie et al. 2020).

Currently, identification of the TGN from dMRI tractography data relies on the region of interest (ROI) selection strategy, where trained experts select TGNs in an interactive way by placing ROIs. In the literature, all related studies have applied the expert ROI selection strategy (Kabasawa et al. 2007; Fujiwara et al. 2011; David Qixiang Chen et al. 2011; David Q. Chen et al. 2016; M. Yoshino et al. 2016; Wei et al. 2016; Behan et al. 2017; Coskun et al. 2017; Zolal et al. 2017; Hung et al. 2017; Moon et al. 2018); however, practical problems remain. First, identification of the TGN is sensitive to ROI placement (Xie et al. 2020; Timothée Jacquesson et al. 2018), where selection of the best-performing ROIs is a challenge. In related work, ROI placement is variable across studies, where adopted ROIs include cisternal portion (CP, also called prepontine cistern, cisternal segment or midpoint of the cisternal segment), root entry zone (REZ), and/or the Meckel's cave (MC) (Kabasawa et al. 2007; Fujiwara et al. 2011; Zolal et al. 2017; Behan et al. 2017; Coskun et al. 2017; David Qixiang Chen et al. 2011; David Q. Chen et al. 2016; Wei et al. 2016; Moon et al. 2018). Second, placement of ROIs can be affected, or even fail, because of imaging artifacts and/or noise at the complex skull base environment (containing nerve, bone, air, soft tissue and cerebrospinal fluid) (Xie et al. 2020). Third, placement of ROIs may require inter-modality registration between dMRI and anatomical MRI (e.g. T2-weighted) data, which is challenging for dMRI with low image resolution (Malinsky et al. 2013) and echo-planar imaging (EPI) distortions (Albi et al. 2018). While ROI placement for TGN identification can be done using dMRI data directly (Fujiwara et al. 2011; Kabasawa et al. 2007; Behan et al. 2017; Moon et al. 2018; Xie et al. 2020), most studies have obtained ROIs from high-resolution anatomical MRI images for a better tissue contrast, requiring a co-registration to the low-resolution dMRI space (Fujiwara et al. 2011; David Qixiang Chen et al. 2011; Krishna et al. 2016; M. Yoshino et al. 2016; David Q. Chen et al. 2016; Hung et al. 2017; Zolal et al. 2017; Coskun et al. 2017). Fourth, ROI placement depends critically on the experience of trained experts and hence inter-observer variability is a real and ongoing issue of accurate image interpretation (Black et al. 2015). Last but not least, manual interpretation is also time-consuming, inefficient and has clinical and expert labor costs.

In neuroscience, there has been an enduring interest in automated image processing and interpretation to resolve inter-observer variability and improve clinical efficiency, e.g., automatically locating brain anatomical structures and functions with references to common atlas spaces (Fischl 2012; Maldjian et al. 2003). There are voxel-wise atlases that enable automated identification of cranial nerves in terms of the presence at a particular location in the brain (Fischl 2012; Sultana 2017; Kikinis et al. 1996). However, these atlases cannot be used automatically identify tractography fibers belonging to the cranial nerves. In brain white matter analysis, many studies have worked on creating brain dMRI tractography atlases (Maddah et al. 2005; O'Donnell and Westin 2007; Ziyan et al. 2009; Yoo et al. 2015; Guevara et al. 2017; Román et al. 2017; Fan Zhang, Wu, et al. 2018). These studies have shown success for automated identification of anatomical white

matter fiber tracts (e.g. arcuate fasciculus), with several advantages including 1) consistent tract identification in the dMRI data from different acquisition protocols, 2) using dMRI data only, thus not requiring inter-modality registration, and 3) high efficiency to reduce expert labor costs and enable tractography analysis in large-scale dMRI datasets. However, we have found no existing studies for automated identification of the cranial nerves, especially the TGN, in tractography.

In this study, we present what we believe is the first study to create a dMRI tractography TGN atlas for automated identification of the TGN, without relying on expert ROI placement. Our method relies on a well-established groupwise fiber clustering pipeline from our research group (O'Donnell and Westin 2007; O'Donnell et al. 2012), which has been successfully applied in multiple research studies (O'Donnell et al. 2017; Gong et al. 2018; Fan Zhang, Wu, et al. 2018; Fan Zhang, Savadjiev, et al. 2018; Wu et al. 2018; Fan et al. 2019; Stojanovski et al. 2019) and has been used recently for creation of an anatomically curated white matter tract atlas (Fan Zhang, Wu, et al. 2018; Fan Zhang et al. 2019). In the present study, we employ this fiber clustering pipeline to identify common TGN structures in an atlas population, including 50 subjects from the Human Connectome Project (HCP) (Van Essen et al. 2013) that provide high-quality dMRI data. Leveraging population-based brain anatomical information and expert neuroanatomical knowledge, we identify a total of 40 fiber clusters belonging to the TGN in the atlas. Each cluster represents a certain anatomical subdivision of the TGN and its variability in the atlas population. The curated TGN model includes not only the cisternal portion but also the putative mesencephalic tract (Shigenaga et al. 1989) and the putative spinal cord tract of V (M. Yoshino et al. 2016), which are important portions of the TGN but have been relatively less studied. The created TGN atlas and the fiber clustering pipeline also provide a method to automatically identify the TGN in new subject datasets. We demonstrate a successful application to dMRI datasets from two different acquisition sites, including those from a clinical acquisition protocol (a lower spatial resolution than the HCP data). The fiber clustering pipeline is open source[1] and the TGN atlas will be made available online, as part of the SlicerDMRI project[2] (Norton et al. 2017).

In the rest of the paper, we first describe the datasets used in this study, followed by the creation of the proposed TGN atlas from 50 healthy adults. Then, we demonstrate our method with an application of the atlas to dMRI datasets that were scanned at two different acquisition sites (with different spatial and angular resolutions). Quantitative and qualitative evaluations are performed to evaluate our method's TGN identification performance, with comparison to expert selected TGNs.

2. Methods

2.1 Datasets and data processing

2.1.1 Datasets

In this study, we used dMRI data from two acquisition sites, including the HCP database (Van Essen et al. 2013) and the Parkinson's Progression Markers Initiative (PPMI) (Marek et al. 2011) database. The HCP data was used for the TGN atlas creation (50 atlas subjects) and experimental evaluation (another 50 testing subjects), while the PPMI data (20 subjects) was used only for experimental evaluation.

The HCP provides dMRI data that was acquired with a high quality image acquisition protocol using a customized Connectome Siemens Skyra scanner and processed using a well-designed processing pipeline

[1] https://github.com/SlicerDMRI/whitematteranalysis
[2] https://dmri.slicer.org/

(Glasser et al. 2013) including motion correction, eddy current correction and EPI distortion correction. The acquisition parameters of the dMRI data in HCP were: TE=89.5 ms, TR=5520 ms, and voxel size=1.25x1.25x1.25 mm^3. A total of 288 images were acquired in each dMRI dataset, including 18 baseline images with a low diffusion weighting b=5 s/mm^2 and 270 diffusion-weighted (DW) images evenly distributed at three shells of b=1000/2000/3000 s/mm^2. More detailed information about the HCP data acquisition and preprocessing can be found in (Glasser et al. 2013). In our study, we used the single-shell b=1000 s/mm^2 data to perform TGN tracking (see Section 2.1.2 for tractography details) because it represents the clinical acquisition protocol and was shown in our previous study to be more effective for TGN identification than higher b values (Xie et al. 2020). We also used the anatomical T2w data for evaluation of the TGNs. The acquisition parameters used for the T2w data were TE=565 ms, TR=3200 ms, and voxel size=0.7x0.7x0.7 mm^3. Imaging data from a total of 100 HCP subjects was used in our study, including 50 subjects for the TGN atlas creation and another 50 subjects for experimental evaluation. We note that to ensure high quality TGN representations for atlas creation, we selected 50 atlas subjects whose dMRI data did not have apparent imaging artifacts and/or noise. (In our previous work (Xie et al. 2020), we showed that manual TGN identification failed in several of the 100 HCP subjects because of imaging artifacts and/or noise at the skull base region.)

The PPMI data was used to test TGN identification performance using a different acquisition protocol than HCP. The acquisition parameters of the dMR data were: TE=88 ms, TR=7600 ms, voxel size=2x2x2 mm^3, 1 baseline image with b=0 s/mm^2 and 64 DW images with b=1000 s/mm^2. T2-weighted data (co-registered with the dMR data) was also used for TGN experimental evaluation. The acquisition parameters for the T2w data were: TE=101 ms, TR=3000 ms, and voxel size=1×1×1 mm^3. The dMRI data was pre-processed with the following steps. Eddy current-induced distortion correction and motion correction were conducted using the Functional Magnetic Resonance Imaging of the Brain (FMRIB) Software Library tool (Jenkinson et al. 2012). An echo-planar imaging (EPI) distortion correction was performed with reference to the T2-weighted image using the Advanced Normalization Tools (ANTS) (Avants, Tustison, and Song 2009). For each subject, a nonlinear registration (registration was restricted to the phase encoding direction) was computed from the b0 image to the T2w image to make an EPI corrective warp. Then, the warp was applied to each diffusion image. Data from 20 PPMI subjects (10 healthy controls and 10 Parkinson's disease patients) was used in our experiment.

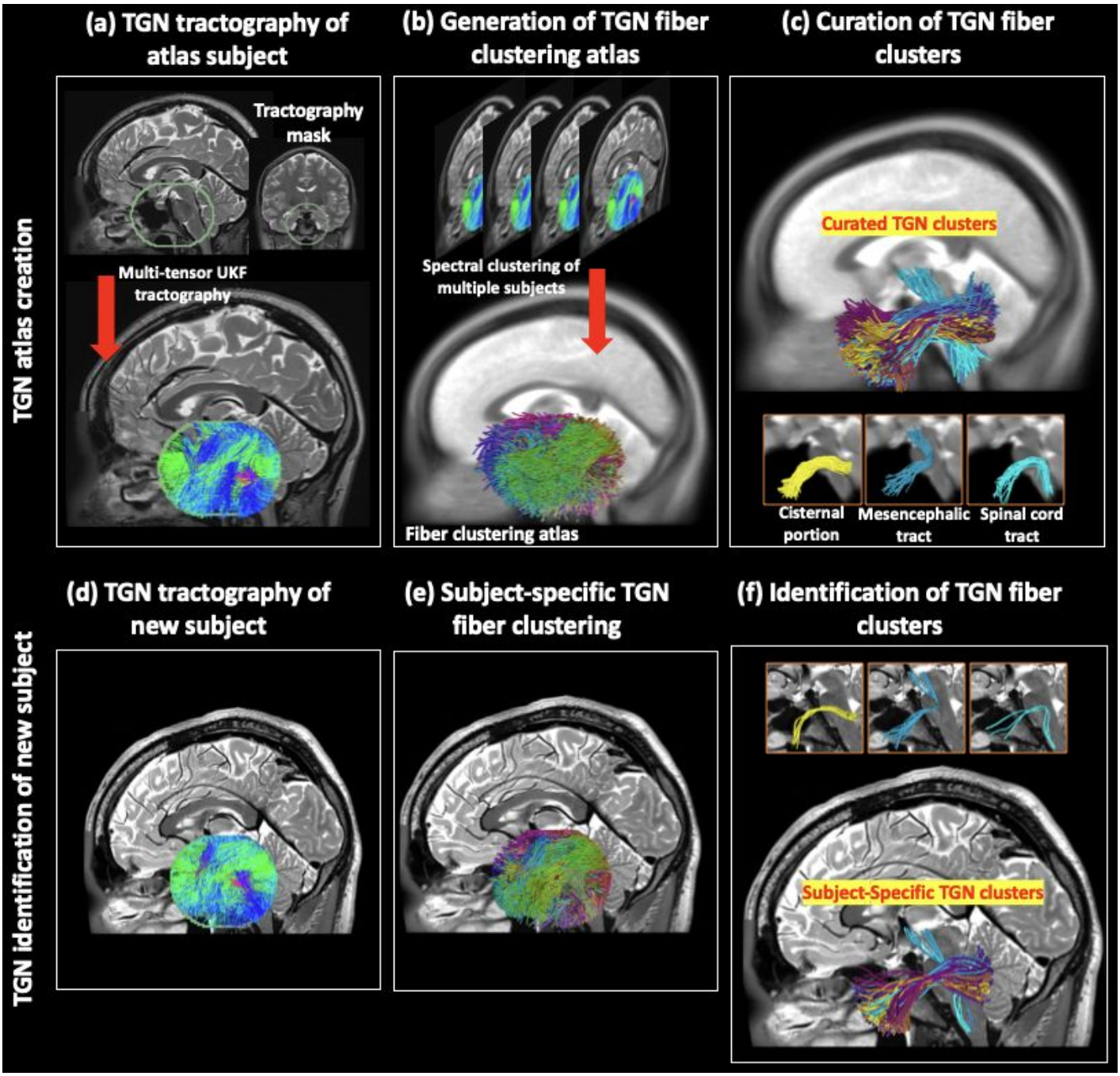

Figure 1. Method overview. (a) to (c) show the creation of the TGN atlas. (a) Multi-tensor tractography is seeded within a mask that covers the possible region through which the TGN passes. (b) Given the tractography data (co-registered to a common space, i.e., the atlas space) from the 50 atlas subjects, spectral clustering is performed to generate a fiber clustering atlas, where each cluster has a unique color. (c) Using expert neuroanatomical knowledge, 40 clusters were identified to belong to the TGN, where each cluster represents a specific subdivision of the whole TGN. Three example clusters are displayed, belonging to the cisternal portion, the mesencephalic trigeminal tract, and the spinal cord tract, respectively. (d) to (f) show identification of the TGN of a new subject. (d) TGN tractography of the new subject is performed, in the same way as the atlas subjects. (e) Fiber clustering of the tractography data (registered to the atlas space) is conducted according to the fiber clustering atlas. (f) Identification of the TGN clusters in the new subject is conducted by finding the corresponding subject-specific clusters to those annotated in the atlas. Three example subject-specific TGN clusters, corresponding to the ones shown in (c), are displayed.

2.1.2 Multi-tensor TGN tractography

For each subject under study, we performed TGN tractography from the dMRI data. We used the two-tensor unscented Kalman filter (UKF) tractography method[3] (Malcolm, Shenton, and Rathi 2010; Reddy and Rathi 2016) to perform TGN tracking, as illustrated in Figure 1(a). We chose the two-tensor UKF tractography method because it has been demonstrated to be effective in tracking the TGN in our previous study (Xie et al. 2020), as well as tracking the brain white matter fiber tracts (Fan Zhang, Wu, et al. 2018; Z. Chen et al. 2016; Gong et al. 2018; Liao et al. 2017). In contrast to other methods that fit a model to the signal independently at each voxel (Qazi et al. 2009; Behan et al. 2017), in the UKF framework each tracking step employs prior information from the previous step to help stabilize model fitting.

TGN tractography was seeded from all voxels within a mask, which was larger than the possible region through which the TGN passes. This procedure was similar to whole brain seeding but it was restricted to the potential TGN region for efficiency. We note that our method does not require sophisticated masking as long as the mask covers the TGN and is approximately in a similar place across all subjects. We used the 3D Slicer Segment Editor tool to do this by placing a spherical or oval mask with a diameter about 35mm, centered at the anterior portion of the pons (as illustrated in Figure 1(a)). Related UKF tractography parameters[4] were well tuned and were set as: *seedingFA* = 0.06, *stoppingFA* = 0.05, *stoppingThreshold* = 0.06, *Qm* = 0.001 and *Ql* = 300. Two seeds per voxel were used for seeding the tractography, which resulted in about 70,000 fibers in the TGN tractography per subject. Visual and quantitative quality control of the tractography data was performed using the quality control tool in the *whitematteranalysis*[5] software.

2.1.3 Manual selection of TGN

For selected subjects, we performed manual ROI-based TGN selection from the tractography data. The manually selected TGNs were used for initial selection of fiber clusters potentially belonging to the TGN in the atlas (see Section 2.2.1) and experimental evaluation (see Section 2.4). We note that for identification of the TGN in new subjects using our method, there is no need to perform manual TGN selection.

We performed manual TGN selection using two ROIs from the MC and the CP of the TGN, as described in (Xie et al. 2020). In brief, the ROI in MC was drawn on the mean b=0 image from the coronal view, and the ROI in CP was drawn on the mean directionally encoded color (DEC) map of diffusion tensor imaging (DTI) from the coronal view. For the HCP data, we attempted to perform manual TGN selection on all of the 100 subjects; however, 8 testing subjects failed because their dMRI data had artifacts and/or noise at the skull base region that prevented placement of ROIs. (We note that we also attempted to draw ROIs on the T2w image, on which the ROIs could be recognized. However, this attempt also failed because the imaging artifacts and/or noise affected the registration between the dMRI and T2w data at the skull base region.) For the PPMI database, we performed manual TGN identification on two randomly selected subjects (a 69 year old female healthy control and a 72 year old male Parkinson's disease patient).

---

[3] https://github.com/pnlbwh/ukftractography

[4] There are five major parameters of the UKF method, including *seedingFA*, *stoppingFA*, *stoppingThreshold, Qm* and *Ql.* These parameters function as follows. Tractography is seeded in all voxels within a provided mask where fractional anisotropy (FA) is greater than *seedingFA.* Tracking stops in voxels where the FA value falls below *stoppingFA* or the sum of the normalized signal across all gradient directions falls below *stoppingThreshold* (a parameter to distinguish between white/gray matter and cerebrospinal fluid (CSF) regions). During the tracking, the UKF method uses *Qm* to control process noise for angles/direction, and *Ql* to control process noise for eigenvalues.

[5] https://github.com/SlicerDMRI/whitematteranalysis

2.2. Creation of TGN atlas

We created the TGN atlas using the tractography data from the 50 atlas subjects. This involved *1)* generating a data-driven fiber clustering atlas for TGN tractography parcellation into multiple fiber clusters and *2)* curating fiber clusters anatomically belonging to the TGN, as illustrated in Figure 1(b,c).

2.2.1 Generation of TGN fiber clustering atlas

The TGN fiber clustering atlas was generated using groupwise fiber clustering to simultaneously parcellate TGN tractography from multiple subjects (Figure 1(b)). First, the TGN tractography data of the 50 atlas subjects was registered into a common space (i.e. atlas space). This was done by performing an affine registration between the b=0 image of each subject (moving image) and a population-mean T2-weighted image (reference image) using 3D Slicer. The obtained transform was then applied to the subject-specific TGN tractography data. The population-mean T2 image (as shown in Figure 1(b)) was provided in the white matter atlas from our group (Fan Zhang, Wu, et al. 2018).

Next, spectral clustering was used to compute a high-dimensional fiber clustering atlas (O'Donnell and Westin 2007) to divide the TGN tractography into *K* clusters, where *K* is a user-given parameter to define the parcellation scale. The spectral embedding created a space that robustly represented each fiber according to its affinity to all other fibers across subjects. The fiber affinity was computed by converting pairwise fiber geometric distances (the popular mean closest point distance is used (Moberts, Vilanova, and van Wijk 2005; O'Donnell and Westin 2007)) using a Gaussian-like kernel, representing fiber similarity according to the fiber geometry and trajectory. Nystrom sampling (Fowlkes et al. 2004) was used to reduce the computations considering the large number of fiber pairs across subjects. Bilateral clustering, simultaneously segmenting TGN fibers on both sides of the cranial base to improve parcellation robustness (O'Donnell and Westin 2007), was applied to obtain the *K* fiber clusters. These computations were performed using the *whitematteranalysis* software, with the suggested settings for related parameters. 10,000 fibers were randomly sampled from each subject's TGN tractography for a total of 0.5 million fibers for the atlas creation.

We generated multiple fiber clustering atlases to investigate the TGN tractography parcellation at different scales (number of clusters, *K*, ranging from 500 to 3000). The TGN atlas consisting of *K*=2500 clusters was chosen because it represented the minimum scale to identify the putative mesencephalic portion of the TGN. The putative mesencephalic tract was a small TGN structure with fewer fibers than the TGN cisternal portion. Using a coarser parcellation scale (e.g. *K*=2000), the putative mesencephalic tract was clustered together with other TGN structures. On the other hand, while using a finer parcellation scale (e.g. *K*=3000) could also provide a reasonable TGN clustering result, it would increase the workload for expert curation of the TGN clusters and decrease parcellation consistency (i.e. consistent identification of each individual cluster) across subjects as suggested in our previous work (Fan Zhang, Wu, et al. 2018; F. Zhang et al. 2017).

2.2.2 Curation of TGN fiber clusters

Given the chosen TGN fiber clustering atlas (*K*=2500), each fiber cluster was annotated to indicate whether it belongs to the TGN or not. This fiber cluster annotation was performed by an initial cluster annotation computation, followed by expert judgment (GX who is a practicing neurosurgeon).

We leveraged the manually selected TGNs to perform an initial selection of potential clusters belonging to the TGN. The purpose of this initial computation step is to bootstrap the expert cluster annotation with a first

pass that can be performed automatically by the computer. From the 10,000 fibers that were randomly sampled from each subject's TGN tractography for the atlas generation, we first identified the fibers that were manually selected to be the TGNs. Then, in the atlas, we calculated a probability for each cluster belonging to the TGN, i.e., the number of fibers that were manually selected to belong to the TGN divided by the number of total fibers in the cluster. We initially selected the fiber clusters that had a probability over 0, which resulted in a total of 127 candidate clusters for expert judgment.

Next, an expert rater (GX who is a practicing neurosurgeon) performed expert annotation of the 127 candidate clusters. Specifically, the expert rater viewed each atlas fiber cluster with reference to the population-mean T2 image that was used to register all atlas TGN tractography into the atlas space (Section 2.2). This enabled viewing of the nerve structure and its variability across all atlas subjects. To confirm the population-based decision, the corresponding subject-specific clusters from five randomly selected subjects was checked with reference to the subject's T2-weighted image.

Overall, there are a total of 40 TGN clusters in the atlas (Figure 1(c)). Each cluster represents a certain anatomical subdivision of the TGN, including the TGN cisternal portion (35 clusters), the putative mesencephalic tract (2 clusters), and the putative spinal cord tract (3 clusters) (example clusters are shown in Figure 1(c)).

2.3 Application of the TGN atlas to new subjects

Identification of the TGN of a new subject was conducted by performing fiber clustering on the subject's TGN tractography, as illustrated in Figure 1(d,e,f). First, the TGN tractography was registered into the atlas space, by performing an affine registration between the subject's b=0 image and the population-mean T2-weighted image and then applying the obtained transform to the TGN tractography data. (This was the same process as registering the TGN tractography data of the atlas subjects.) Then, subject-specific fiber clusters were detected using spectral embedding of the registered tractography, followed by assignment of each fiber to the closest atlas cluster (O'Donnell and Westin 2007). Outlier fibers were removed if their fiber affinity regarding the atlas cluster was over 2 standard deviations from the cluster's mean fiber affinity (as applied in (O'Donnell et al. 2017; Fan Zhang, Wu, et al. 2018)). As a result, the new subject's TGN tractography was divided into multiple fiber clusters, where each cluster corresponded to a certain atlas fiber cluster. Next, TGN identification of the new subject was conducted by automatically finding the subject-specific clusters that corresponded to the annotated atlas clusters.

2.4 Experimental evaluation

All subjects' TGN tractography (including the 50 HCP atlas subjects, the 50 HCP testing subjects and the 20 PPMI subjects) was parcellated using the proposed atlas. Then, we performed the following experiments to evaluate the TGN identification performance of our method.

2.4.1 TGN identification rate

We computed the mean TGN identification rate (percentage of successfully identified TGNs) across all subjects in each dataset. We performed this evaluation for the overall TGN, as well as for the subdivisions including the cisternal portion, the mesencephalic tract and the spinal cord tract. The identified TGNs and their subdivisions were confirmed (i.e., visually assessed as belonging to the TGN) by the expert rater (GX). We reported the mean identification rate of the 50 HCP atlas subjects (a total of 100 TGNs), that of the 50 HCP testing subjects (a total of 100 TGNs), and that of the 20 PPMI testing subjects (a total of 40 TGNs). For

comparison, we also reported the mean TGN identification rates of the expert TGN selection in the 50 HCP atlas subjects and in the 50 HCP testing subjects.

2.4.2 TGN spatial overlap

We performed a quantitative comparison to assess if the identified TGNs using the atlas spatially overlapped with the manually identified TGNs. Specifically, we computed the weighted Dice (wDice) coefficient between the automatically and manually identified TGNs from the same subject. wDice coefficient was designed specifically for measuring volumetric overlap of fiber tracts (Cousineau et al. 2017; Fan Zhang et al. 2019). wDice extends the standard Dice coefficient (Dice 1945) taking account of the number of fibers per voxel so that it gives higher weighting to voxels with dense fibers. For the HCP database, we reported the mean and the standard deviation of the wDice values across the 50 atlas subjects and those across the 42 testing subjects with successful manual TGN selection. (Note that the other 8 HCP testing subjects were not included in the quantitative comparison because manual selection failed.) For the PPMI database, we reported the wDice score for each of the two selected subjects with manually selected TGNs.

2.4.3 TGN visualization

For visual comparison of the automated TGN identification and the manual selection, we rendered the automatically and manually identified TGNs from three example subjects. These included one HCP testing subject with successful manual TGN identification, one HCP testing subject with unsuccessful manual TGN identification, and one PPMI testing subject (healthy control).

We then provided a visualization of TGNs to show the anatomical regions where the TGN passed. We first showed the curated TGN in the atlas. This was done by rendering a voxel-based fiber density heatmap that quantifies the number of fibers present in each voxel and the regions through which the TGN passed on the population-mean T2-weighted image (used for co-registering the TGN tractography data). We also showed subject-specific TGNs, by rendering their fiber density heatmaps and the regions through which the TGN passed on the corresponding subject T2w images. Three example subjects (the same subjects as used in the above visual comparison) were used in this visualization.

3. Results

3.1 TGN identification rate

All TGNs were successfully identified using the proposed automated identification method in all subjects under study, including the 50 HCP atlas subjects, the 50 HCP testing subjects (including the 8 subjects where manual selection failed), and the 20 PPMI testing subjects. Regarding the different subdivisions, the cisternal portion was identified in all subjects under study. We also obtained high identification rates for the mesencephalic tract (on average 50.0%) and spinal cord tract (on average 52.4%) across all 100 HCP subjects, where the manual selection could successfully identify 34.5% of the mesencephalic tracts and 37.0% of the spinal cord tracts. For the PPMI data, the identification rates of the mesencephalic tract and spinal cord tract using the proposed automated method were relatively low compared to those in the HCP data.

Table 1. TGN identification rate (percentage of successfully identified TGNs) of the overall TGN and its subdivisions

using the proposed automated identification method (highlighted in gray) and the manual selection method. For the PPMI data, we did not perform manual TGN identification; thus, the TGN identification rate was not reported.

		Overall		TGN cisternal portion		Mesencephalic trigeminal tract		The spinal cord tract	
		Automated	Manual	Automated	Manual	Automated	Manual	Automated	Manual
HCP atlas subjects (n=50)		100%	100%	100%	100%	45.0%	40.0%	59.0%	35.0%
HCP testing subjects (n = 50)	With successful manual identification (n = 42)	100%	100%	100%	100%	58.3%	34.5%	47.7%	46.4%
	With unsuccessful manual identification (n = 8)	100%	0%	100%	0%	37.5%	0%	31.3%	0%
20 PPMI testing subjects		100%	--	100%	--	7.5%	--	22.5%	--

3.2 TGN spatial overlap

Table 2 gives the mean and the standard deviation of the wDice scores across the 50 HCP atlas subjects and those of the 42 HCP testing subjects with successful manual TGN identification. High mean wDice scores, on average over 0.75, were obtained. The threshold for a good wDice score to evaluate tract spatial overlap was suggested to be 0.72 according to Cousineau et al (Cousineau et al. 2017). Table 2 also gives the wDice scores of the two PPMI testing subjects with manually selected TGNs, which were about 0.79 for both subjects.

Table 2. Spatial overlap (wDice score) between automatically (proposed) and manually identified TGNs.

50 HCP atlas subjects		0.7585 ± 0.0883
42 HCP testing subjects (with successful manual identification)		0.7534 ± 0.1127
PPMI testing subjects	Subject 1	0.7892
	Subject 2	0.7887

3.3 TGN visualization

Figure 2 gives a visual comparison between the automatically (proposed) and manually identified TGNs for the three example subjects. Highly visually comparable results were obtained between the two methods for

the two subjects with successful manual identification. Our proposed method could also successfully identify a visually reasonable TGN on the subject where manual identification failed.

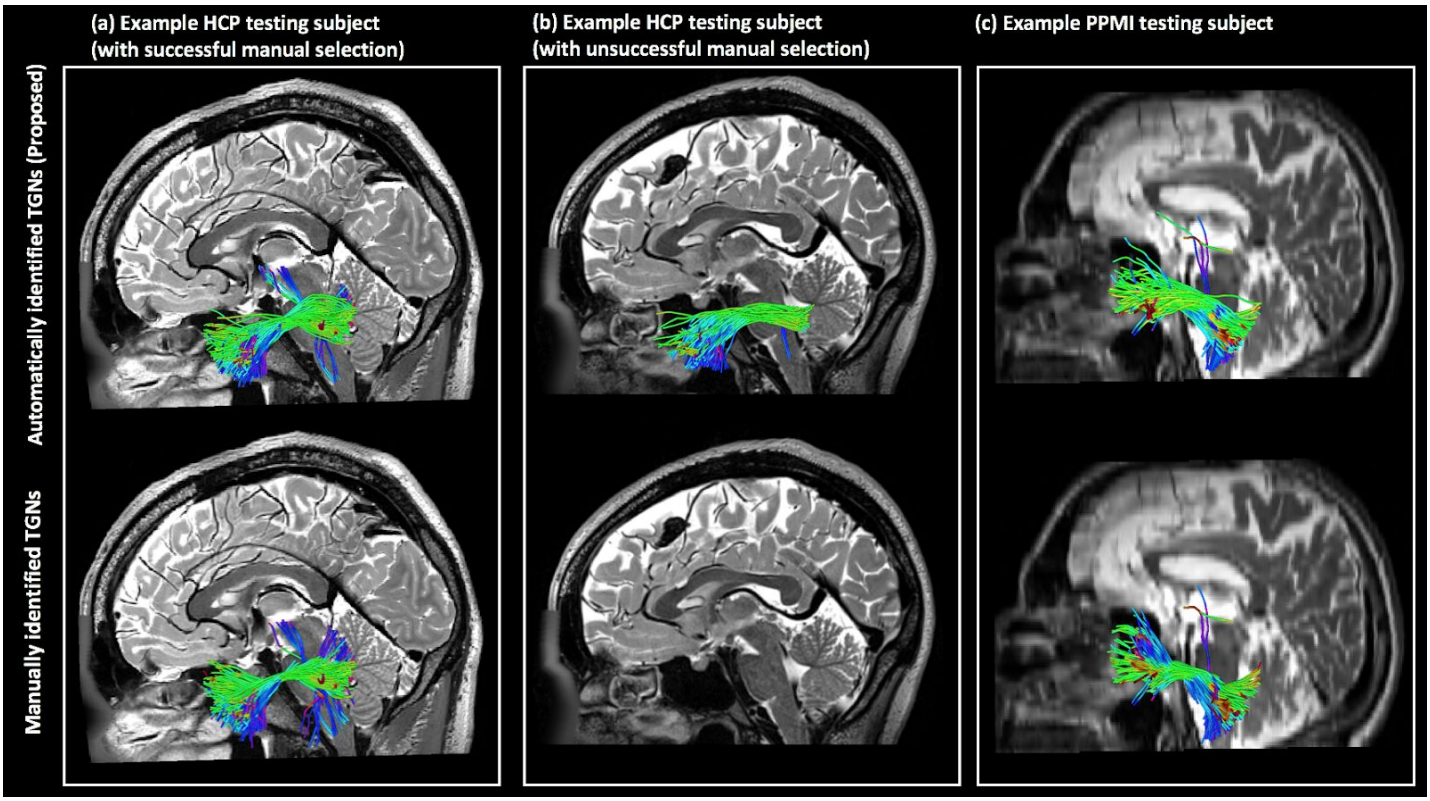

Figure 2. Visual comparison of the TGN 3D fiber trajectory between the automatically (proposed) and manually identified TGNs. The three example subjects include one HCP testing subject with successful manual TGN identification, one HCP testing subject with unsuccessful manual TGN identification, and one PPMI testing subject (healthy control).

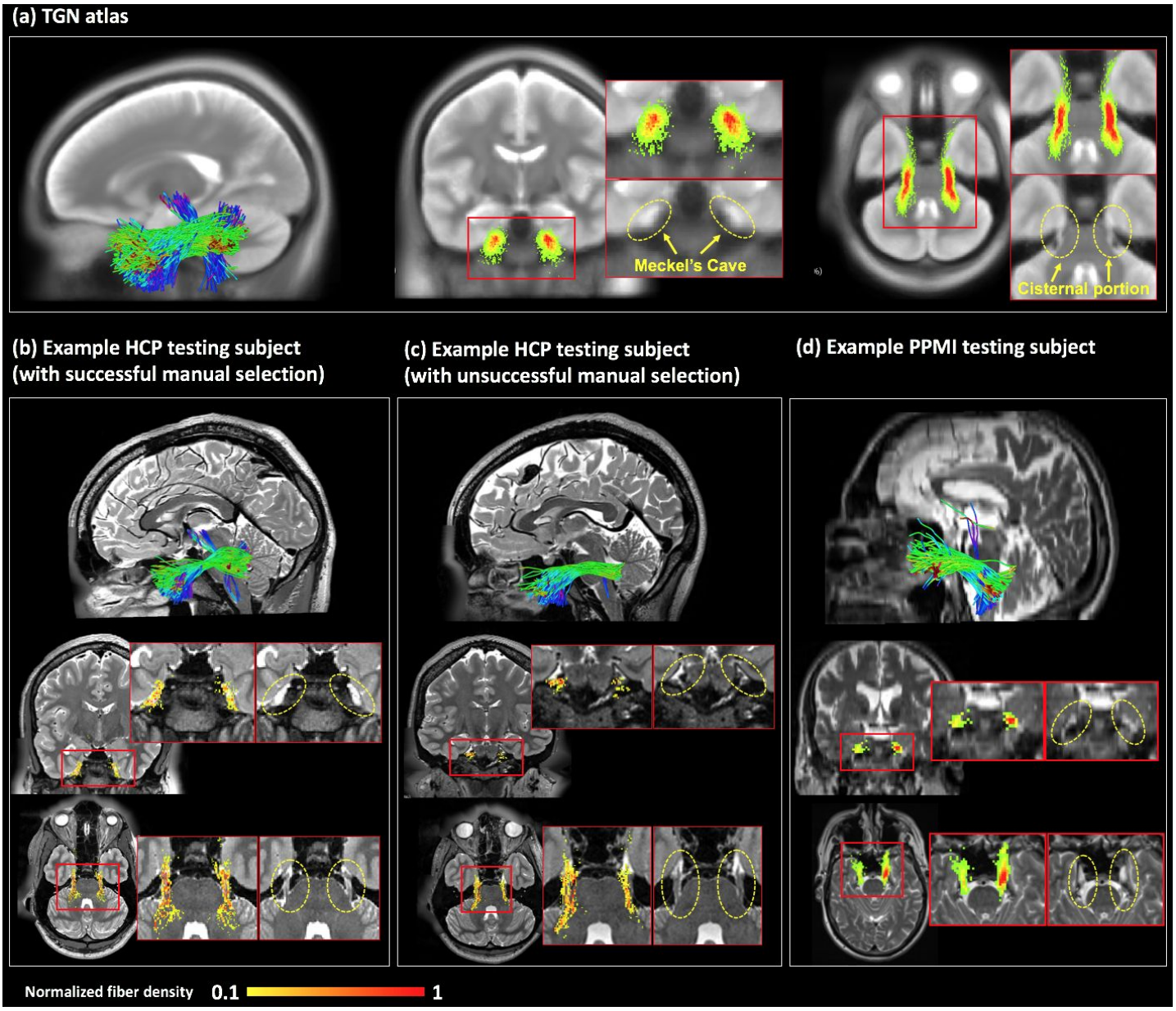

Figure 3. Visualization of the TGN 3D fiber trajectory and the voxel-based fiber density map, overlaid on T2w data. (a) The TGN in the atlas, overlaid on the population mean T2w image. (b, c) Subject-specific TGNs of the two HCP subjects, overlaid on the corresponding T2w images. (d) Subject-specific TGNs of the example PPMI subject (healthy control), overlaid on the corresponding T2w image. For each sub-figure, inset images are provided for better visualization of the regions where the TGN passes through. The value of a voxel in the heatmaps represents the number of fibers that have fibers passing through the voxel. For visualization of the fiber density map at the same scale, each map is normalized by the maximal value on the map for each sub-figure.

Figure 3(a) shows the 3D fiber trajectory and the fiber density map of the TGN curated in the atlas, overlaid on the population mean T2w image. In general, the TGN had an anatomically correct shape and corresponded well to the known anatomy of the TGN pathways, i.e., passing through the Meckel's Cave (MC) and overlapping well with the cisternal portion (CP), as appearing on the T2w image. Figure 3(b) gives the TGN visualization of the example HCP subject with successful manual selection. The TGNs identified using our method were anatomically correct, passing through the MC and overlapping with the CP as appearing on

the T2w image. Figure 3(c) renders the identified TGNs from the example HCP subject with unsuccessful manual selection. In this subject, our obtained TGNs are visually anatomically correct in terms of the shape; however, they do not pass through the MC and do not overlap with the CP as appearing on the T2w data. This was because the dMRI data of this subject had imaging artifacts in the skull base region, which affected the registration with the T2w data at the skull base region. (This also explained the failure of our attempt to perform manual selection using ROIs drawn on the T2w data.) Figure 3(d) displays the TGNs identified from the example PPMI subject. The identified TGNs were anatomically correct, passing through the MC and overlapping with the CP as appearing on the T2w data.

4. Discussion

In this paper, we present a TGN tractography fiber clustering atlas to enable automated identification of TGN from dMRI tractography. We show not only highly comparable TGN identification performance of our method with comparison to expert TGN identification but also several advantages. First, our method performed automated TGN identification, without required expert ROI placement; thus, it provides an efficient tool to reduce expert labor costs and inter-operator bias. Second, our method was robust to potential imaging artifacts and/or noise and thus obtained a higher successful TGN identification rate. We have several overall observations about the results, which are discussed below.

We demonstrated successful applications of the TGN atlas for subject-specific TGN identification, where 100% of the TGNs of all subjects under study were successfully identified. Importantly, our method could successfully identify the TGNs of the 8 HCP testing subjects where manual TGN selection failed. In our work, we found that manual ROI placement was affected by imaging artifacts and/or noise at the skull base region from two aspects. First, ROIs could not be drawn because the anatomical structures of interest were not visible on the noisy dMRI data. Second, ROIs from inter-modality imaging (e.g. anantomcal T2w) could not be applied because of bad image registration at the skull base region. Our method identified the TGNs from dMRI tractography directly, without relying on the success of ROI placement. Therefore, our method provided a robust tool for TGN identification, in spite of the potential imaging artifacts and/or noise at the skull base region.

We showed the proposed atlas's high TGN identification performance despite the heterogeneity of the dMRI data, specifically in the dMRI with relatively low spatial resolution. Our testing data included the dMRI data from the PPMI database, which was independently acquired using a different scanning protocol and processed in a different manner compared to the HCP data. These factors could affect the tractography results and thus influence the identification generalizations between different dMRI datasets. However, despite any potential effects from the heterogeneity of the dMRI data, we showed excellent TGN identification generalization performance across the multiple testing datasets. One important contributing factor was the application of the two-tensor UKF tractography (Malcolm, Shenton, and Rathi 2010; Reddy and Rathi 2016) which is highly sensitive and robust in fiber tracking in dMRI data from different acquisition protocols.

The proposed atlas enabled identification of subdivisions of the TGNs. The TGN covers an extensive nerve distribution territory, including several segments such as the cisternal portion, the mesencephalic trigeminal tract, and the spinal cord tract (Joo et al. 2014; Go, Kim, and Zee 2001). Unlike the cisternal portion of TGN that have been studied in multiple previous works, the mesencephalic tract and spinal cord tract are relatively less studied. The mesencephalic tract is an important portion of the TGN that conveys proprioceptive information from the teeth, masticatory muscles and temporomandibular joints (Shigenaga et al. 1989). The spinal cord tract is important for mapping the pain-temperature sensory functions of the face, mouth and nose (Grant and Arvidsson 1975). While we showed good performance on identifying the mesencephalic tract and

spinal cord tract, we noticed that the identification of these substructures could be affected by the image quality. In the PPMI data, we found a lower identification rate of these two tracts compared to the high-quality and high-resolution HCP data. This result suggested that improving the imaging acquisition would be helpful for identification of the more comprehensive anatomy of the TGN.

We demonstrated the anatomical validity of the proposed atlas. The automatically identified TGNs were highly comparable to the manual TGN selection results and corresponded well to the known anatomy, passing through the MC and overlapping with the CP, as appearing on the T2w image. False positive fibers have been shown to be dominant in tractography data (Maier-Hein et al. 2017). In particular, in the application of tractography to identify TGNs, multiple studies have identified anatomically unexpected false positive fibers (M. Yoshino et al. 2016; Behan et al. 2017; David Qixiang Chen et al. 2011; Timothée Jacquesson et al. 2018; David Q. Chen et al. 2016; Hung et al. 2017; Xie et al. 2020). In our method, we included expert judgment to ameliorate potential false positive fibers by excluding false positive clusters in the atlas, e.g. the ones entering the temporal lobe. The fiber clustering pipeline also included a data-driven false positive fiber removal for rejection of fibers that have improbable fiber geometric trajectory (O'Donnell et al. 2017; Fan Zhang, Wu, et al. 2018). These two processing steps largely ameliorate the issue of false positive fibers, while there were still a small amount of false positive fibers, e.g. false positive fibers entering the temporal lobe, the inferior cerebellar peduncle, or the middle cerebellar peduncle.

Potential limitations of the present study, including suggested future work to address limitations, are as follows. First, the aim of this study was to demonstrate the applications of the proposed atlas for automated TGN identification. While we focused on demonstrating successful applications across the different cohorts, we did not perform any statistical analyses for within- or between-cohort studies. Many research studies have suggested that TGNs are important for understanding and/or potential treatment of various neurological disorders such as major depressive disorder, attention-deficit/hyperactivity disorder and Parkinson's disease (Schrader et al. 2011; McGough et al. 2015; Barz et al. 1997). Future research could include an investigation of population-specific characteristics of the TGNs identified using our method. Second, future work could explore the application of the proposed method on brains with tumors and/or lesions near to or involving the TGN. Identification of TGNs has been shown to provide important information for presurgical planning (Timothee Jacquesson et al. 2019). Our previous work has shown successful brain white matter tract identification in brain tumor patients using the same underlying technical methods as in the present study. Future investigation and validation of the proposed atlas on identify TGNs in brain tumor patients are needed. Third, in this study, we applied the UKF tractography method for TGN tracking because it has been demonstrated to be effective in tracking TGNs (Xie et al. 2020). Further work could include an application to the TGN tractography data from other fiber tracking methods such as constrained spherical deconvolution (Jeurissen et al. 2011) and global tractography (Christiaens et al. 2015).

5. Conclusions

In this paper, we have presented an dMRI tractography fiber clustering atlas to enable automated identification of the TGN. Experimental results show successful application of the proposed atlas on dMRI data with different MRI acquisition protocols and demonstrate advantages over traditional manual selection strategy.

ACKNOWLEDGMENTS:

We gratefully acknowledge funding provided by the Jennifer Oppenheimer Cancer Research Initiative and the following National Institutes of Health (NIH) grants: P41 EB015902, P41 EB015898, R01 MH074794, R01 MH111917, R01 MH119222, R01 CA235589, HHSN261200800001E and U01 CA199459.

References

Albi, Angela, Antonio Meola, Fan Zhang, Pegah Kahali, Laura Rigolo, Chantal M. W. Tax, Pelin Aksit Ciris, et al. 2018. “Image Registration to Compensate for EPI Distortion in Patients with Brain Tumors: An Evaluation of Tract-Specific Effects.” *Journal of Neuroimaging: Official Journal of the American Society of Neuroimaging* 28 (2): 173–82.

Avants, Brian B., Nick Tustison, and Gang Song. 2009. “Advanced Normalization Tools (ANTS).” *The Insight Journal* 2: 1–35.

Balestrino, M., and M. Leandri. 1997. “Trigeminal Neuralgia in Pontine Ischaemia.” *Journal of Neurology, Neurosurgery, and Psychiatry* 62 (3): 297–98.

Barz, S., T. Hummel, E. Pauli, M. Majer, C. J. Lang, and G. Kobal. 1997. “Chemosensory Event-Related Potentials in Response to Trigeminal and Olfactory Stimulation in Idiopathic Parkinson’s Disease.” *Neurology* 49 (5): 1424–31.

Basser, P. J., J. Mattiello, and D. LeBihan. 1994. “MR Diffusion Tensor Spectroscopy and Imaging.” *Biophysical Journal* 66 (1): 259–67.

Basser, P. J., S. Pajevic, C. Pierpaoli, J. Duda, and A. Aldroubi. 2000. “In Vivo Fiber Tractography Using DT-MRI Data.” *Magnetic Resonance in Medicine: Official Journal of the Society of Magnetic Resonance in Medicine / Society of Magnetic Resonance in Medicine* 44 (4): 625–32.

Behan, Brendan, David Q. Chen, Francesco Sammartino, Danielle D. DeSouza, Erika Wharton-Shukster, and Mojgan Hodaie. 2017. “Comparison of Diffusion-Weighted MRI Reconstruction Methods for Visualization of Cranial Nerves in Posterior Fossa Surgery.” *Frontiers in Neuroscience* 11 (October): 554.

Black, David F., David R. DeLone, Timothy J. Kaufmann, Patrick D. Fitz-Gibbon, Rickey E. Carter, Mary M. Machulda, and Kirk M. Welker. 2015. “Retrospective Analysis of Interobserver Spatial Variability in the Localization of Broca’s and Wernicke's Areas Using Three Different fMRI Language Paradigms.” *Journal of Neuroimaging: Official Journal of the American Society of Neuroimaging* 25 (4): 626–33.

Casselman, Jan, Koen Mermuys, Joost Delanote, Johan Ghekiere, and Kenneth Coenegrachts. 2008. “MRI of the Cranial Nerves—More than Meets the Eye: Technical Considerations and Advanced Anatomy.” *Neuroimaging Clinics of North America* 18 (2): 197–231.

Chen, David Q., Danielle D. DeSouza, David J. Hayes, Karen D. Davis, Paul O’Connor, and Mojgan Hodaie. 2016. “Diffusivity Signatures Characterize Trigeminal Neuralgia Associated with Multiple Sclerosis.” *Multiple Sclerosis* 22 (1): 51–63.

Chen, David Qixiang, Jessica Quan, Abhijit Guha, Michael Tymianski, David Mikulis, and Mojgan Hodaie. 2011. “Three-Dimensional in Vivo Modeling of Vestibular Schwannomas and Surrounding Cranial Nerves with Diffusion Imaging Tractography.” *Neurosurgery* 68 (4): 1077–83.

Chen, Zhenrui, Yanmei Tie, Olutayo Olubiyi, Fan Zhang, Alireza Mehrtash, Laura Rigolo, Pegah Kahali, et al. 2016. “Corticospinal Tract Modeling for Neurosurgical Planning by Tracking through Regions of Peritumoral Edema and Crossing Fibers Using Two-Tensor Unscented Kalman Filter Tractography.” *International Journal of Computer Assisted Radiology and Surgery* 11 (8): 1475–86.

Christiaens, Daan, Marco Reisert, Thijs Dhollander, Stefan Sunaert, Paul Suetens, and Frederik Maes. 2015. “Global Tractography of Multi-Shell Diffusion-Weighted Imaging Data Using a Multi-Tissue Model.” *NeuroImage* 123 (December): 89–101.

Ciftci, E., Yonca Anik, Arzu Arslan, Gur Akansel, Tahsin Sarisoy, and Ali Demirci. 2004. “Driven Equilibrium (drive) MR Imaging of the Cranial Nerves V-VIII: Comparison with the T2-Weighted 3D TSE Sequence.” *European Journal of Radiology* 51 (3): 234–40.

Coskun, Ozlem, Murat Ucar, Doga Vuralli, Funuzar Yildirim, Rumeysa Cetinkaya, Suna Akin Takmaz, and Serap Ucler. 2017. “MR Tractography in Short Lasting Unilateral Neuralgiform Headache Attacks with

Conjunctival Injection and Tearing (SUNCT) Patients: Case Reports." *Pain Medicine* 18 (7): 1377–81.

Cousineau, Martin, Pierre-Marc Jodoin, Félix C. Morency, Verena Rozanski, Marilyn Grand'Maison, Barry J. Bedell, and Maxime Descoteaux. 2017. "A Test-Retest Study on Parkinson's PPMI Dataset Yields Statistically Significant White Matter Fascicles." *NeuroImage. Clinical* 16 (July): 222–33.

Delitala, A., A. Brunori, and F. Chiappetta. 1999. "Trigeminal Neuralgia Resulting from Infarction of the Root Entry Zone of the Trigeminal Nerve: Case Report." *Neurosurgery*.

Dice, Lee R. 1945. "Measures of the Amount of Ecologic Association Between Species." *Ecology* 26 (3): 297–302.

Fan, D., N. N. Chaudhari, K. A. Rostowsky, M. Calvillo, S. K. Lee, N. F. Chowdhury, F. Zhang, L. J. O'Donnell, and A. Irimia. 2019. "Post-Traumatic Cerebral Microhemorrhages and Their Effects Upon White Matter Connectivity in the Aging Human Brain." In *2019 41st Annual International Conference of the IEEE Engineering in Medicine and Biology Society (EMBC)*, 198–203.

Fischl, Bruce. 2012. "FreeSurfer." *NeuroImage* 62 (2): 774–81.

Fowlkes, Charless, Serge Belongie, Fan Chung, and Jitendra Malik. 2004. "Spectral Grouping Using the Nyström Method." *IEEE Transactions on Pattern Analysis and Machine Intelligence* 26 (2): 214–25.

Fujiwara, Shunrou, Makoto Sasaki, Tsukasa Wada, Kohsuke Kudo, Ryonoshin Hirooka, Daiya Ishigaki, Yasumasa Nishikawa, Ayumi Ono, Mao Yamaguchi, and Kuniaki Ogasawara. 2011. "High-Resolution Diffusion Tensor Imaging for the Detection of Diffusion Abnormalities in the Trigeminal Nerves of Patients with Trigeminal Neuralgia Caused by Neurovascular Compression." *Journal of Neuroimaging: Official Journal of the American Society of Neuroimaging* 21 (2): e102–8.

Glasser, Matthew F., Stamatios N. Sotiropoulos, J. Anthony Wilson, Timothy S. Coalson, Bruce Fischl, Jesper L. Andersson, Junqian Xu, et al. 2013. "The Minimal Preprocessing Pipelines for the Human Connectome Project." *NeuroImage* 80 (October): 105–24.

Go, J. L., P. E. Kim, and C. S. Zee. 2001. "The Trigeminal Nerve." *Seminars in Ultrasound, CT, and MR* 22 (6): 502–20.

Golby, Alexandra J., Alexander Norbash, and Gerald D. Silverberg. 1998. "Trigeminal Neuralgia Resulting from Infarction of the Root Entry Zone of the Trigeminal Nerve: Case Report." *Neurosurgery* 43 (3): 620–23.

Gong, Shun, Fan Zhang, Isaiah Norton, Walid I. Essayed, Prashin Unadkat, Laura Rigolo, Ofer Pasternak, et al. 2018. "Free Water Modeling of Peritumoral Edema Using Multi-Fiber Tractography: Application to Tracking the Arcuate Fasciculus for Neurosurgical Planning." *PloS One* 13 (5): e0197056.

Grant, G., and J. Arvidsson. 1975. "Transganglionic Degeneration in Trigeminal Primary Sensory Neurons." *Brain Research* 95 (2-3): 265–79.

Guevara, Miguel, Claudio Román, Josselin Houenou, Delphine Duclap, Cyril Poupon, Jean François Mangin, and Pamela Guevara. 2017. "Reproducibility of Superficial White Matter Tracts Using Diffusion-Weighted Imaging Tractography." *NeuroImage* 147 (February): 703–25.

Hung, Peter S-P, David Q. Chen, Karen D. Davis, Jidan Zhong, and Mojgan Hodaie. 2017. "Predicting Pain Relief: Use of Pre-Surgical Trigeminal Nerve Diffusion Metrics in Trigeminal Neuralgia." *NeuroImage. Clinical* 15 (June): 710–18.

Ishida Go, Oishi Makoto, Fukuda Masafumi, Sato Mitsuya, and Fujii Yukihiko. 2011. "[Depiction of the trigeminal nerve deviated by a tumor lesion, using probabilistic diffusion tensor tractography]." *No shinkei geka. Neurological surgery* 39 (3): 255–62.

Jacquesson, Timothée, Carole Frindel, Gabriel Kocevar, Moncef Berhouma, Emmanuel Jouanneau, Arnaud Attyé, and Francois Cotton. 2018. "Overcoming Challenges of Cranial Nerve Tractography: A Targeted Review." *Neurosurgery*, July. https://doi.org/10.1093/neuros/nyy229.

Jacquesson, Timothee, Fang-Chang Yeh, Sandip Panesar, Jessica Barrios, Arnaud Attyé, Carole Frindel, Francois Cotton, Paul Gardner, Emmanuel Jouanneau, and Juan C. Fernandez-Miranda. 2019. "Full Tractography for Detecting the Position of Cranial Nerves in Preoperative Planning for Skull Base Surgery: Technical Note." *Journal of Neurosurgery*. https://doi.org/10.3171/2019.1.jns182638.

Jannetta, Peter J. 1967. "Arterial Compression of the Trigeminal Nerve at the Pons in Patients with Trigeminal Neuralgia." *Journal of Neurosurgery*. https://doi.org/10.3171/jns.1967.26.1part2.0159.

Jenkinson, Mark, Christian F. Beckmann, Timothy E. J. Behrens, Mark W. Woolrich, and Stephen M. Smith.

2012. “FSL.” *NeuroImage* 62 (2): 782–90.
Jeurissen, Ben, Alexander Leemans, Derek K. Jones, Jacques-Donald Tournier, and Jan Sijbers. 2011. “Probabilistic Fiber Tracking Using the Residual Bootstrap with Constrained Spherical Deconvolution.” *Human Brain Mapping* 32 (3): 461–79.
Joo, Wonil, Fumitaka Yoshioka, Takeshi Funaki, Koji Mizokami, and Albert L. Rhoton Jr. 2014. “Microsurgical Anatomy of the Trigeminal Nerve.” *Clinical Anatomy* 27 (1): 61–88.
Kabasawa, Hiroyuki, Yoshitaka Masutani, Shigeki Aoki, Osamu Abe, Tomohiko Masumoto, Naoto Hayashi, and Kuni Ohtomo. 2007. “3T PROPELLER Diffusion Tensor Fiber Tractography: A Feasibility Study for Cranial Nerve Fiber Tracking.” *Radiation Medicine* 25 (9): 462–66.
Kikinis, Ron, Martha E. Shenton, Robert M. Donnino, Ferenc A. Jolesz, Dan V. Iosifescu, Robert W. McCarley, Pairash Saiviroonporn, et al. 1996. “A Digital Brain Atlas for Surgical Planning, Model-Driven Segmentation, and Teaching.” *IEEE Transactions on Visualization and Computer Graphics*, no. 3: 232–41.
Krishna, Vibhor, Francesco Sammartino, Philip Yee, David Mikulis, Matthew Walker, Gavin Elias, and Mojgan Hodaie. 2016. “Diffusion Tensor Imaging Assessment of Microstructural Brainstem Integrity in Chiari Malformation Type I.” *Journal of Neurosurgery* 125 (5): 1112–19.
Liao, Ruizhi, Lipeng Ning, Zhenrui Chen, Laura Rigolo, Shun Gong, Ofer Pasternak, Alexandra J. Golby, Yogesh Rathi, and Lauren J. O’Donnell. 2017. “Performance of Unscented Kalman Filter Tractography in Edema: Analysis of the Two-Tensor Model.” *NeuroImage. Clinical* 15 (June): 819–31.
Love, S., and H. B. Coakham. 2001. “Trigeminal Neuralgia: Pathology and Pathogenesis.” *Brain: A Journal of Neurology* 124 (Pt 12): 2347–60.
Maddah, Mahnaz, Andrea U. J. Mewes, Steven Haker, W. Eric L. Grimson, and Simon K. Warfield. 2005. “Automated Atlas-Based Clustering of White Matter Fiber Tracts from DTMRI.” *Medical Image Computing and Computer-Assisted Intervention: MICCAI ... International Conference on Medical Image Computing and Computer-Assisted Intervention* 8 (Pt 1): 188–95.
Maier-Hein, Klaus H., Peter F. Neher, Jean-Christophe Houde, Marc-Alexandre Côté, Eleftherios Garyfallidis, Jidan Zhong, Maxime Chamberland, et al. 2017. “The Challenge of Mapping the Human Connectome Based on Diffusion Tractography.” *Nature Communications* 8 (1): 1349.
Malcolm, James G., Martha E. Shenton, and Yogesh Rathi. 2010. “Filtered Multitensor Tractography.” *IEEE Transactions on Medical Imaging* 29 (9): 1664–75.
Maldjian, Joseph A., Paul J. Laurienti, Robert A. Kraft, and Jonathan H. Burdette. 2003. “An Automated Method for Neuroanatomic and Cytoarchitectonic Atlas-Based Interrogation of fMRI Data Sets.” *NeuroImage* 19 (3): 1233–39.
Malinsky, Milos, Roman Peter, Erlend Hodneland, Astri J. Lundervold, Arvid Lundervold, and Jiri Jan. 2013. “Registration of FA and T1-Weighted MRI Data of Healthy Human Brain Based on Template Matching and Normalized Cross-Correlation.” *Journal of Digital Imaging* 26 (4): 774–85.
Marek, Kenneth, Danna Jennings, Shirley Lasch, Andrew Siderowf, Caroline Tanner, Tanya Simuni, Chris Coffey, et al. 2011. “The Parkinson Progression Marker Initiative (PPMI).” *Progress in Neurobiology* 95 (4): 629–35.
McGough, James J., Sandra K. Loo, Alexandra Sturm, Jennifer Cowen, Andrew F. Leuchter, and Ian A. Cook. 2015. “An Eight-Week, Open-Trial, Pilot Feasibility Study of Trigeminal Nerve Stimulation in Youth with Attention-Deficit/hyperactivity Disorder.” *Brain Stimulation* 8 (2): 299–304.
Moberts, B., A. Vilanova, and J. J. van Wijk. 2005. “Evaluation of Fiber Clustering Methods for Diffusion Tensor Imaging.” In *VIS 05. IEEE Visualization, 2005.*, 65–72.
Moon, Hyeong Cheol, Soon-Tae You, Hyeon Man Baek, Young Jai Jeon, Chan-A Park, Jei Jun Cheong, Youn Joo Lee, and Young Seok Park. 2018. “7.0 Tesla MRI Tractography in Patients with Trigeminal Neuralgia.” *Magnetic Resonance Imaging* 54 (January): 265–70.
Norton, Isaiah, Walid Ibn Essayed, Fan Zhang, Sonia Pujol, Alex Yarmarkovich, Alexandra J. Golby, Gordon Kindlmann, et al. 2017. “SlicerDMRI: Open Source Diffusion MRI Software for Brain Cancer Research.” *Cancer Research* 77 (21): e101–3.
O’Donnell, Lauren J., Yannick Suter, Laura Rigolo, Pegah Kahali, Fan Zhang, Isaiah Norton, Angela Albi, et al. 2017. “Automated White Matter Fiber Tract Identification in Patients with Brain Tumors.” *NeuroImage.*

Clinical 13: 138–53.

O'Donnell, Lauren J., William M. Wells III, Alexandra J. Golby, and Carl-Fredrik Westin. 2012. "Unbiased Groupwise Registration of White Matter Tractography." In *Medical Image Computing and Computer-Assisted Intervention – MICCAI 2012*, edited by Nicholas Ayache, Hervé Delingette, Polina Golland, and Kensaku Mori, 123–30. Lecture Notes in Computer Science 7512. Springer Berlin Heidelberg.

O'Donnell, Lauren J., and Carl-Fredrik Westin. 2007. "Automatic Tractography Segmentation Using a High-Dimensional White Matter Atlas." *IEEE Transactions on Medical Imaging* 26 (11): 1562–75.

Qazi, Arish A., Alireza Radmanesh, Lauren O'Donnell, Gordon Kindlmann, Sharon Peled, Stephen Whalen, Carl-Fredrik Westin, and Alexandra J. Golby. 2009. "Resolving Crossings in the Corticospinal Tract by Two-Tensor Streamline Tractography: Method and Clinical Assessment Using fMRI." *NeuroImage* 47 Suppl 2 (August): T98–106.

Reddy, Chinthala P., and Yogesh Rathi. 2016. "Joint Multi-Fiber NODDI Parameter Estimation and Tractography Using the Unscented Information Filter." *Frontiers in Neuroscience* 10 (April): 166.

Román, Claudio, Miguel Guevara, Ronald Valenzuela, Miguel Figueroa, Josselin Houenou, Delphine Duclap, Cyril Poupon, Jean-François Mangin, and Pamela Guevara. 2017. "Clustering of Whole-Brain White Matter Short Association Bundles Using HARDI Data." *Frontiers in Neuroinformatics* 11 (December): 73.

Ruiz-Juretschke, Fernando, Laín H. González-Quarante, Roberto García-Leal, and Vicente Martínez de Vega. 2018. "Neurovascular Relations of the Trigeminal Nerve in Asymptomatic Individuals Studied with High-Resolution Three-Dimensional Magnetic Resonance Imaging." *Anatomical Record* , April. https://doi.org/10.1002/ar.23818.

Schrader, Lara M., Ian A. Cook, Patrick R. Miller, Eve R. Maremont, and Christopher M. DeGiorgio. 2011. "Trigeminal Nerve Stimulation in Major Depressive Disorder: First Proof of Concept in an Open Pilot Trial." *Epilepsy & Behavior*. https://doi.org/10.1016/j.yebeh.2011.06.026.

Shigenaga, Y., K. Doe, S. Suemune, Y. Mitsuhiro, K. Tsuru, K. Otani, Y. Shirana, M. Hosoi, A. Yoshida, and K. Kagawa. 1989. "Physiological and Morphological Characteristics of Periodontal Mesencephalic Trigeminal Neurons in the Cat--Intra-Axonal Staining with HRP." *Brain Research* 505 (1): 91–110.

Stojanovski, Sonja, Daniel Felsky, Joseph D. Viviano, Saba Shahab, Rutwik Bangali, Christie L. Burton, Gabriel A. Devenyi, et al. 2019. "Polygenic Risk and Neural Substrates of Attention-Deficit/Hyperactivity Disorder Symptoms in Youths With a History of Mild Traumatic Brain Injury." *Biological Psychiatry* 85 (5): 408–16.

Sultana, Sharmin. 2017. "Development of an Atlas-Based Segmentation of Cranial Nerves Using Shape-Aware Discrete Deformable Models for Neurosurgical Planning and Simulation." Old Dominion University. https://doi.org/10.25777/m30g-bw21.

Tsutsumi, Satoshi, Hideo Ono, Yukimasa Yasumoto, and Hisato Ishii. 2018. "The Trigeminal Root: An Anatomical Study Using Magnetic Resonance Imaging." *Surgical and Radiologic Anatomy: SRA*, September. https://doi.org/10.1007/s00276-018-2106-1.

Van Essen, David C., Stephen M. Smith, Deanna M. Barch, Timothy E. J. Behrens, Essa Yacoub, Kamil Ugurbil, and WU-Minn HCP Consortium. 2013. "The WU-Minn Human Connectome Project: An Overview." *NeuroImage* 80 (October): 62–79.

Wei, Peng-Hu, Zhi-Gang Qi, Ge Chen, Ming-Chu Li, Jian-Tao Liang, Hong-Chuan Guo, Yu-Hai Bao, and Qiang Hao. 2016. "Identification of Cranial Nerves around Trigeminal Schwannomas Using Diffusion Tensor Tractography: A Technical Note and Report of 3 Cases." *Acta Neurochirurgica* 158 (3): 429–35.

Wu, Ye, Fan Zhang, Nikos Makris, Yuping Ning, Isaiah Norton, Shenglin She, Hongjun Peng, et al. 2018. "Investigation into Local White Matter Abnormality in Emotional Processing and Sensorimotor Areas Using an Automatically Annotated Fiber Clustering in Major Depressive Disorder." *NeuroImage* 181 (July): 16–29.

Xie, Guoqiang, Fan Zhang, Laura Leung, Michael A. Mooney, Lorenz Epprecht, Isaiah Norton, Yogesh Rathi, et al. 2020. "Anatomical Assessment of Trigeminal Nerve Tractography Using Diffusion MRI: A Comparison of Acquisition B-Values and Single- and Multi-Fiber Tracking Strategies." *NeuroImage:Clinical*.

Yadav, Yad Ram, Yadav Nishtha, Pande Sonjjay, Parihar Vijay, Ratre Shailendra, and Khare Yatin. 2017. "Trigeminal Neuralgia." *Asian Journal of Neurosurgery* 12 (4): 585–97.

Yoo, Sang Wook, Pamela Guevara, Yong Jeong, Kwangsun Yoo, Joseph S. Shin, Jean-Francois Mangin, and Joon-Kyung Seong. 2015. "An Example-Based Multi-Atlas Approach to Automatic Labeling of White Matter Tracts." *PloS One* 10 (7): e0133337.

Yoshino, Masanori, Kumar Abhinav, Fang-Cheng Yeh, Sandip Panesar, David Fernandes, Sudhir Pathak, Paul A. Gardner, and Juan C. Fernandez-Miranda. 2016. "Visualization of Cranial Nerves Using High-Definition Fiber Tractography." *Neurosurgery* 79 (1): 146–65.

Yoshino, Norio, Hideaki Akimoto, Ichiro Yamada, Tsukasa Nagaoka, Akemi Tetsumura, Tohru Kurabayashi, Eiichi Honda, Shin Nakamura, and Takehito Sasaki. 2003. "Trigeminal Neuralgia: Evaluation of Neuralgic Manifestation and Site of Neurovascular Compression with 3D CISS MR Imaging and MR Angiography." *Radiology* 228 (2): 539–45.

Zhang, Fan, Peter Savadjiev, Weidong Cai, Yang Song, Yogesh Rathi, Birkan Tunç, Drew Parker, et al. 2018. "Whole Brain White Matter Connectivity Analysis Using Machine Learning: An Application to Autism." *NeuroImage* 172 (May): 826–37.

Zhang, Fan, Ye Wu, Isaiah Norton, Yogesh Rathi, Alexandra J. Golby, and Lauren J. O'Donnell. 2019. "Test-Retest Reproducibility of White Matter Parcellation Using Diffusion MRI Tractography Fiber Clustering." *Human Brain Mapping* 40 (10): 3041–57.

Zhang, Fan, Ye Wu, Isaiah Norton, Laura Rigolo, Yogesh Rathi, Nikos Makris, and Lauren J. O'Donnell. 2018. "An Anatomically Curated Fiber Clustering White Matter Atlas for Consistent White Matter Tract Parcellation across the Lifespan." *NeuroImage* 179 (October): 429–47.

Zhang, F., I. Norton, W. Cai, Y. Song, W. M. Wells, and L. J. O'Donnell. 2017. "Comparison between Two White Matter Segmentation Strategies: An Investigation into White Matter Segmentation Consistency." In *2017 IEEE 14th International Symposium on Biomedical Imaging (ISBI 2017)*, 796–99.

Ziyan, Ulas, Mert R. Sabuncu, W. Eric L. Grimson, and Carl-Fredrik Westin. 2009. "Consistency Clustering: A Robust Algorithm for Group-Wise Registration, Segmentation and Automatic Atlas Construction in Diffusion MRI." *International Journal of Computer Vision* 85 (3): 279–90.

Zolal, Amir, Stephan B. Sobottka, Dino Podlesek, Jennifer Linn, Bernhard Rieger, Tareq A. Juratli, Gabriele Schackert, and Hagen H. Kitzler. 2017. "Comparison of Probabilistic and Deterministic Fiber Tracking of Cranial Nerves." *Journal of Neurosurgery* 127 (3): 613–21.